

Supplementary Materials for **Unveiling massive numbers of cancer-related urinary-microRNA candidates via nanowires**

Takao Yasui, Takeshi Yanagida, Satoru Ito, Yuki Konakade, Daiki Takeshita, Tsuyoshi Naganawa, Kazuki Nagashima, Taisuke Shimada, Noritada Kaji, Yuta Nakamura, Ivan Adiyasa Thiodorus, Yong He, Sakon Rahong, Masaki Kanai, Hiroshi Yukawa, Takahiro Ochiya, Tomoji Kawai, Yoshinobu Baba

Published 15 December 2017, *Sci. Adv.* **3**, e1701133 (2017)

DOI: 10.1126/sciadv.1701133

The PDF file includes:

- fig. S1. Schematic of the fabrication procedure for nanowires anchored into PDMS.
- fig. S2. Nanowires anchored into PDMS.
- fig. S3. FESEM images and EDS elemental mappings corresponding to FESEM images for PDMS without nanowires, PDMS with buried nanowires, and nanowire-embedded PDMS; scale bars, 1 μm .
- fig. S4. Mechanical stability of anchored nanowires and nonanchored nanowires.
- fig. S5. Extraction process of miRNAs in urine using the nanowire-anchored microfluidic device, ultracentrifugation, and commercially available kits.
- fig. S6. FESEM images and EDS elemental mappings of an STEM image of a single nanowire.
- fig. S7. Detection of EVs on ZnO nanowires, ZnO/Al₂O₃ core-shell nanowires, and no nanowires using an antibody of CD9.
- fig. S8. Zeta potential of EVs in urine.
- fig. S9. Size distribution of EVs collected by ultracentrifugation and EV-free miRNAs collected onto nanowires.
- fig. S10. Size distribution of the urinary free-floating objects.
- Legend for movie S1
- Legend for data S1

Other Supplementary Material for this manuscript includes the following:
(available at advances.sciencemag.org/cgi/content/full/3/12/e1701133/DC1)

- movie S1 (.mov format). EV collection followed by miRNA extraction in urine using the nanowire-anchored microfluidic device.
- data S1 (Microsoft Excel format). Logarithmic signal intensities in noncancer miRNAs with those in cancer miRNAs.

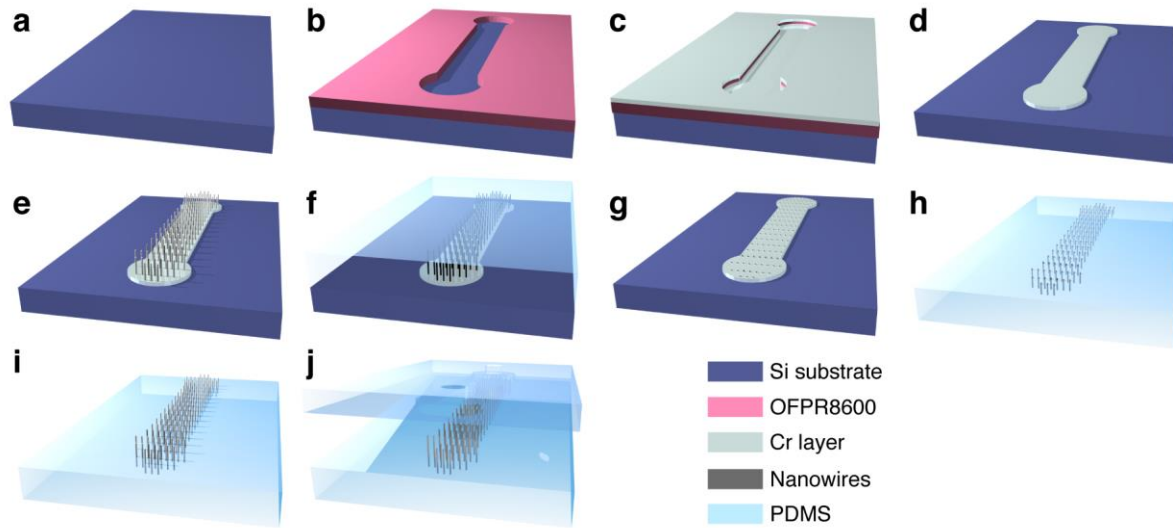


fig. S1. Schematic of the fabrication procedure for nanowires anchored into PDMS. (a-g) The nanowires are anchored into PDMS by utilizing lithographic techniques and a PDMS curing process. Components include Si substrate (dark cyan), OFPR8600 photoresist (pink), Cr layer (faded cyan), nanowires (gray) and PDMS (transparent cyan). (h) A schematic illustration (gray rods, nanowires; transparent cyan areas, PDMS) for buried nanowires after poring, curing and peeling off PDMS. (i) A schematic illustration for growing nanowires from the buried nanowires (nanowire-embedded PDMS). (j) A schematic illustration for bonding the nanowire-embedded PDMS substrate to the microfluidic herringbone-structured PDMS substrate.

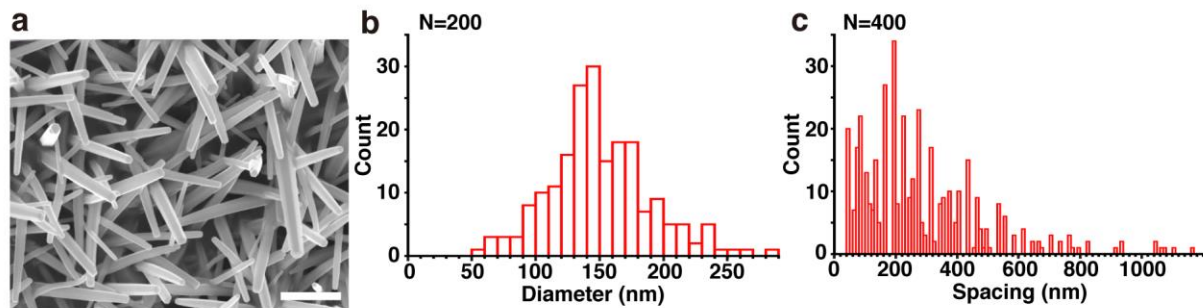


fig. S2. Nanowires anchored into PDMS. (a) An overview FESEM image of the nanowires; scale bar, 1 μm . (b) Diameter distribution of the nanowires. Mean diameter of the nanowires was 150 nm. (c) Spacing distribution between the nanowires. A spacing was defined as the closest spacing between two nanowires, which was measured from cross-sectional SEM images. Mean spacing between the nanowires was 200 nm.

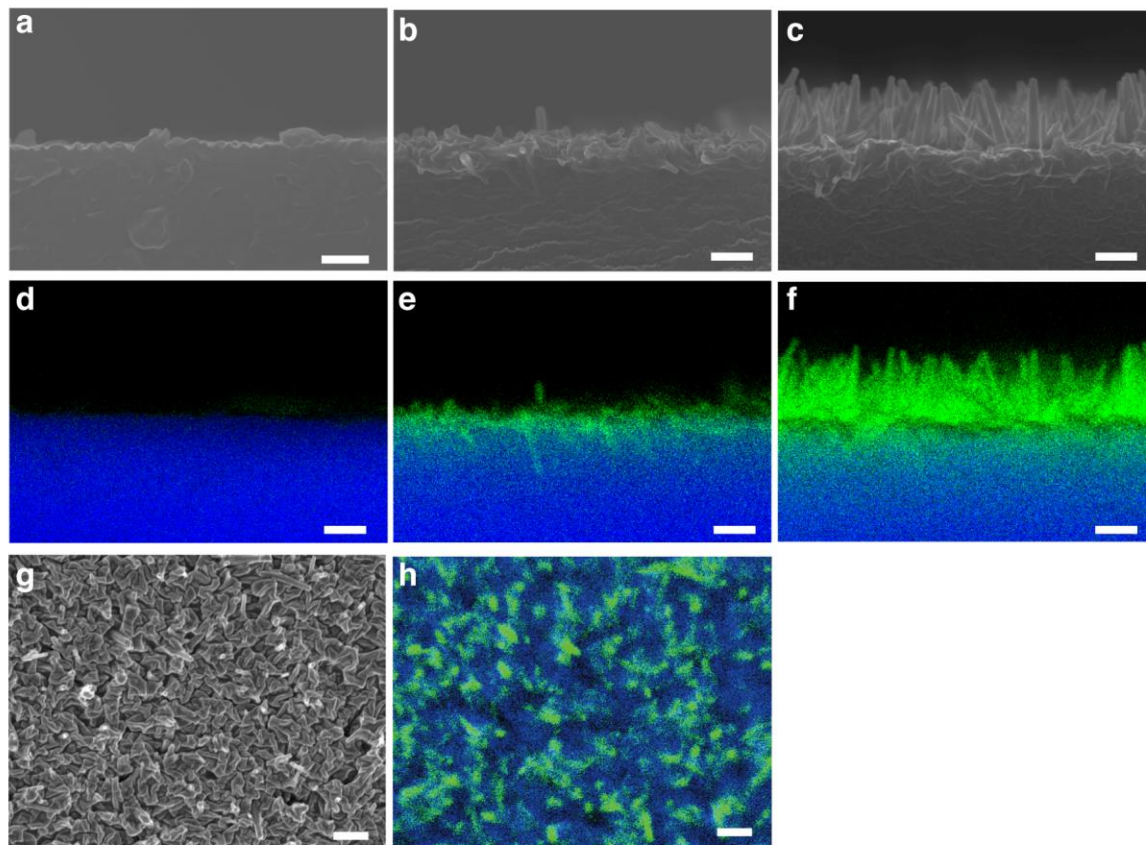


fig. S3. FESEM images and EDS elemental mappings corresponding to FESEM images for PDMS without nanowires, PDMS with buried nanowires, and nanowire-embedded PDMS; scale bars, 1 μm . (a-c) Vertical cross-sectional FESEM images of PDMS without nanowires, PDMS with buried nanowires, and nanowire-embedded PDMS, respectively. (d-f) EDS elemental mappings corresponding to the cross-sectional FESEM images in figs. S2a-c; Si and Zn are highlighted as blue and green. (g) An overview FESEM image of PDMS with buried nanowires. (h) An EDS elemental mapping corresponding to the overview FESEM image in fig. S2g; Si and Zn are highlighted as blue and green.

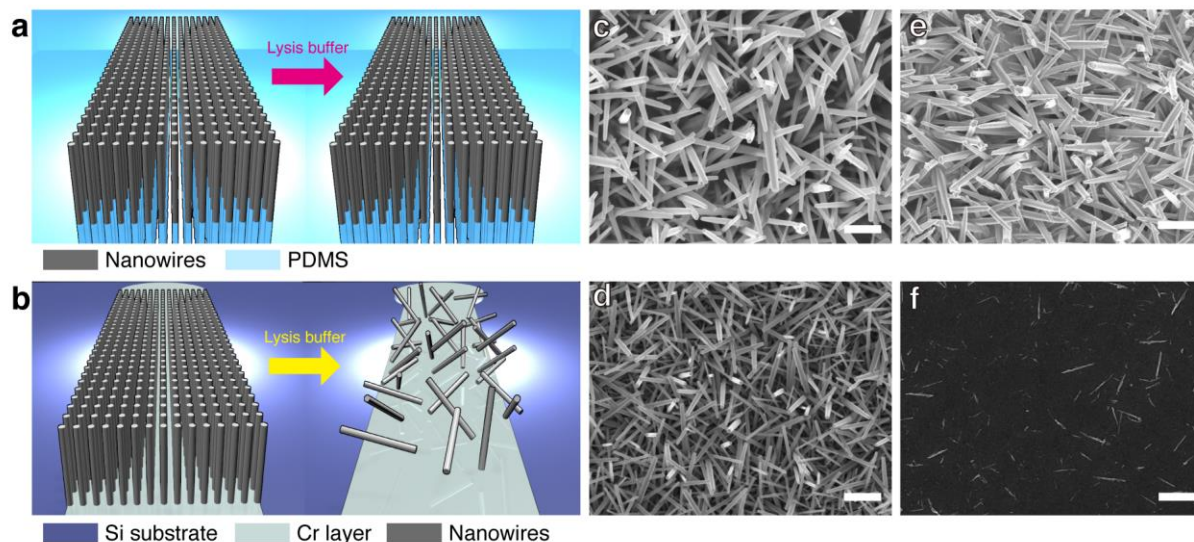


fig. S4. Mechanical stability of anchored nanowires and nonanchored nanowires. (a, b)

Schematic illustrations of the nanowires anchored into PDMS and nanowires on the Si substrate when exposed to lysis buffer. Components include nanowires (gray), PDMS (transparent cyan), Si substrate (dark cyan), and Cr layer (faded cyan). The nonanchored nanowires were fabricated on the thermally oxidized chromium layer on the Si substrate. (c, d) An overview of FESEM images for the nanowires anchored into PDMS and the nanowires on the Si substrate; scale bars, 1 μm . (e, f) An overview of FESEM images for the nanowires anchored into PDMS and the nanowires on the Si substrate when exposed to lysis buffer; scale bars, 1 μm . After exposure to lysis buffer, the nanowires anchored into PDMS did not peel off, while the nonanchored nanowires did.

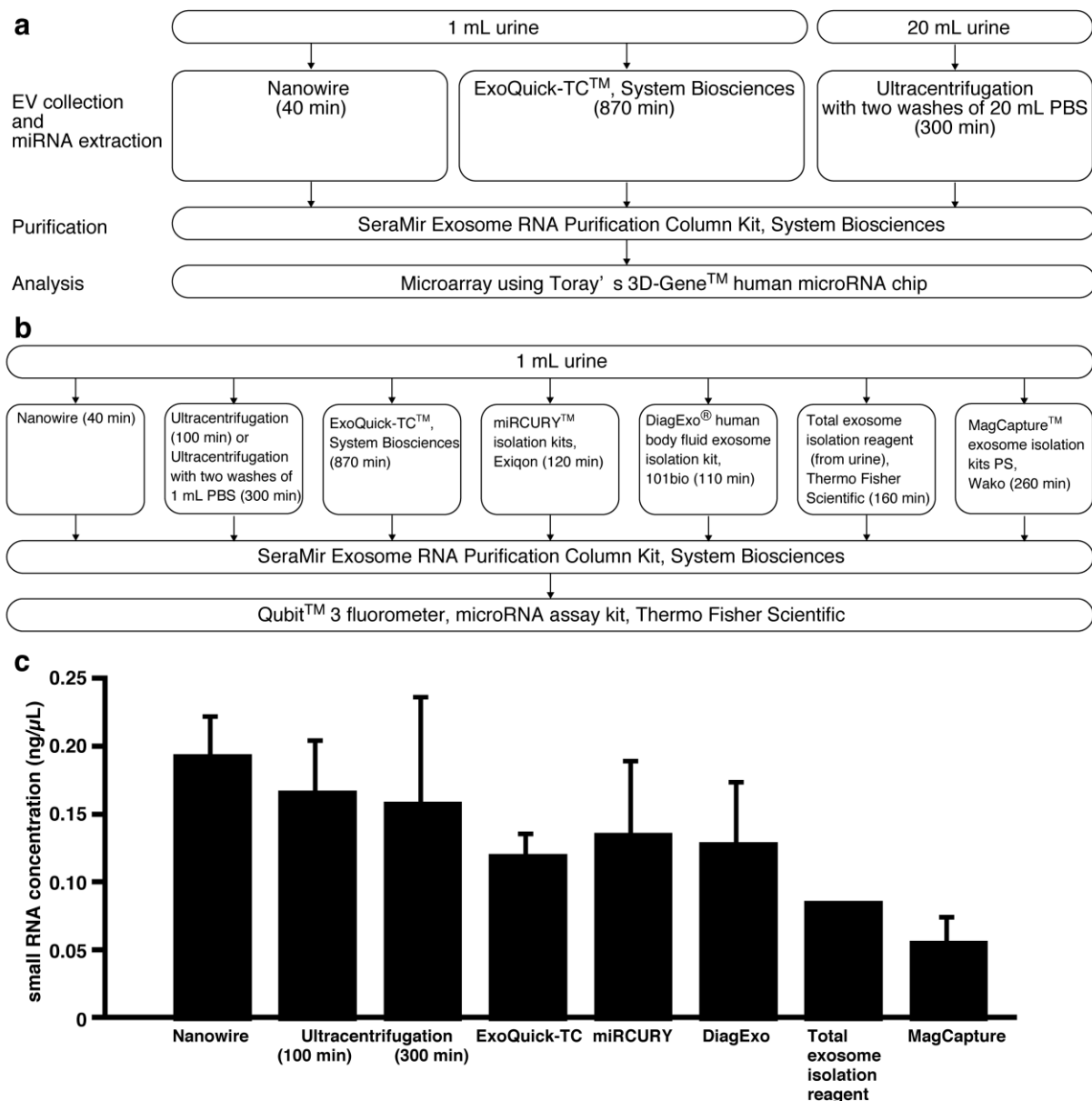


fig. S5. Extraction process of miRNAs in urine using the nanowire-anchored microfluidic device, ultracentrifugation, and commercially available kits. (a) Experimental procedures for microarray analysis of miRNA expression. **(b)** Experimental procedures for small RNA quantification using the Qubit® microRNA assay kit (Thermo Fisher Scientific). After miRNA extraction using each methodology, we performed RNA purification and small RNA quantification. **(c)** Small RNA quantification using each methodology. Since the Qubit® microRNA assay kit could quantify small RNAs (~20 nucleotides or base pairs), not only miRNAs, we used the small RNA concentration as the y-axis. These data implied that the washing step did not affect RNA collection efficiency. Error bars show the standard deviation for a series of measurements ($N \geq 3$).

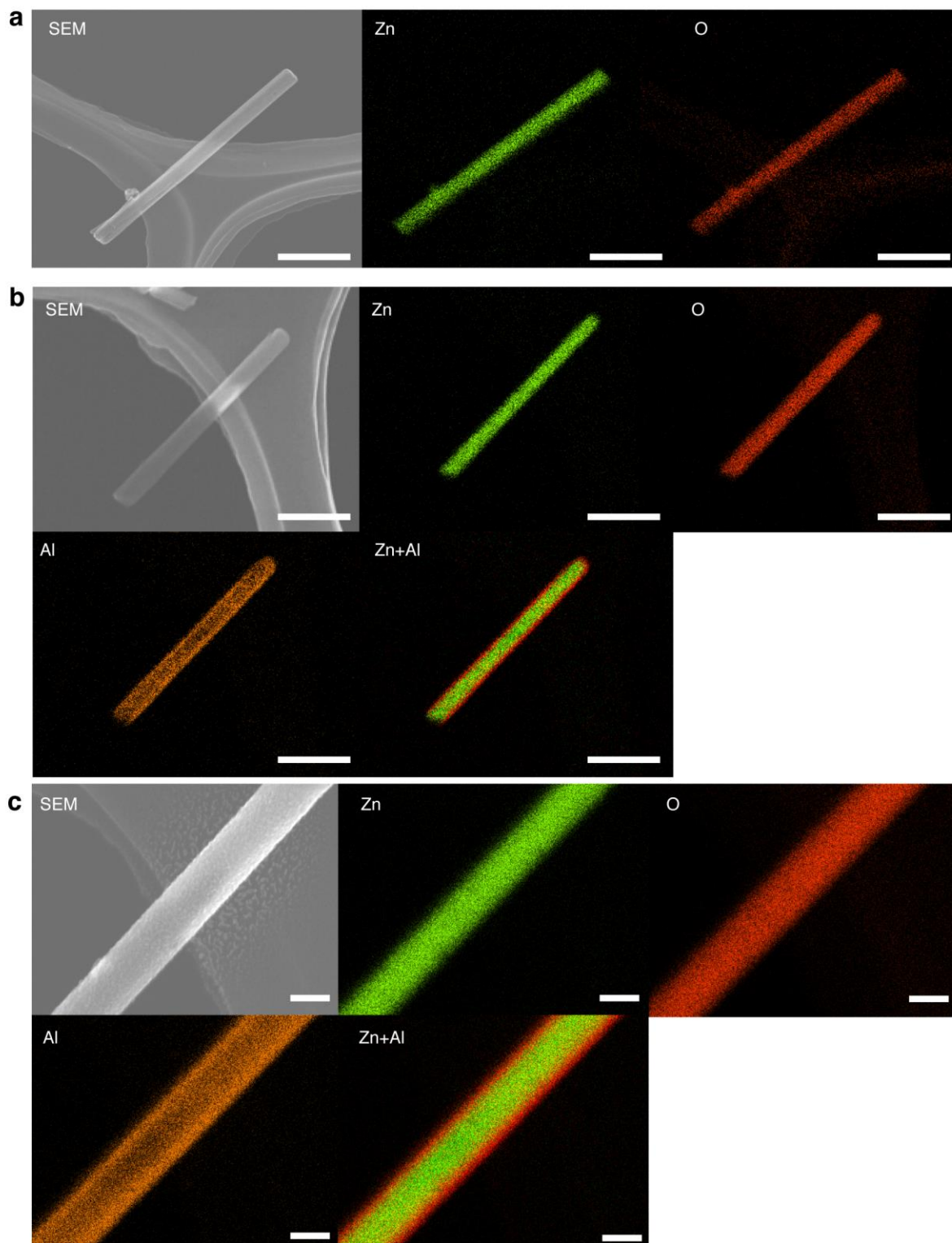


fig. S6. FESEM images and EDS elemental mappings of an STEM image of a single nanowire.

Zn, O, and Al are highlighted as green, red, and orange for single elemental mappings. Zn and Al are highlighted as green and red for dual elemental mappings. (a) A ZnO single nanowire; scale bars, 500 nm. (b) A ZnO/Al₂O₃ core-shell single nanowire; scale bars, 500 nm. (c) A ZnO/Al₂O₃ core-shell single nanowire; scale bars, 100 nm.

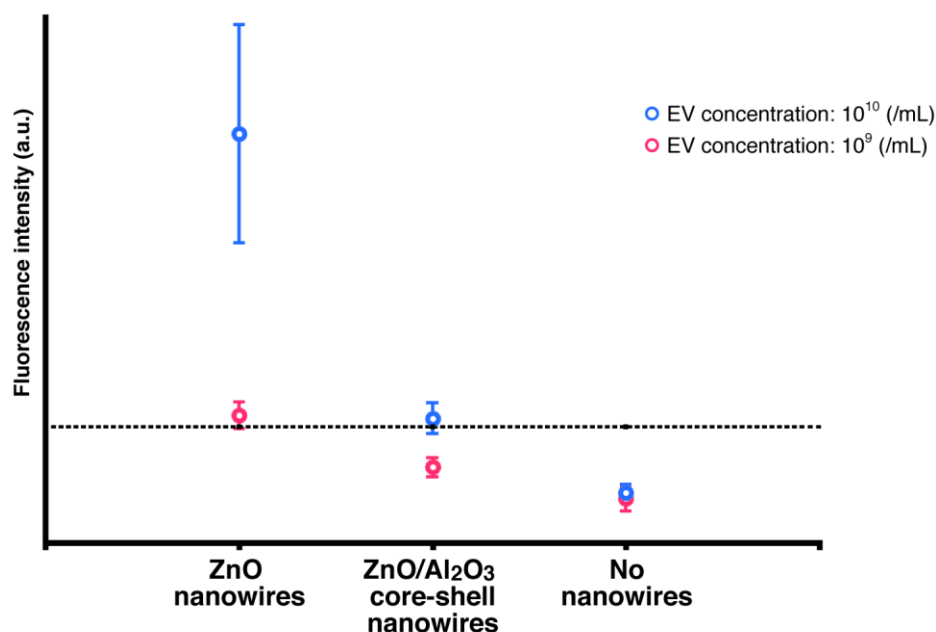


fig. S7. Detection of EVs on ZnO nanowires, ZnO/Al₂O₃ core-shell nanowires, and no nanowires using an antibody of CD9. The black dotted line shows the signal level at 3 standard deviations above the background. Error bars showing the standard deviation for a series of measurements of ZnO nanowires, ZnO/Al₂O₃ core-shell nanowires, and no nanowires (N=40, 24, and 24, respectively). Pink and cyan circles show EV concentrations of 10^9 and 10^{10} particles/mL, respectively. After introduction of EVs, PBS was introduced into three different devices to remove uncollected EVs. The first device had ZnO nanowires, the second had ZnO/Al₂O₃ core-shell nanowires, and the third had no nanowires. Then, we introduced 1% BSA solution into each device and let this stand for 15 min. After washing out each device using PBS, we introduced a mouse monoclonal anti-human CD9 (10 μ g/mL, Abcam, Plc.), which is also a well-known membrane protein expressed on exosomes, into each device, and then let this stand for 15 min. Additionally, we washed out each device using PBS, and introduced a goat polyclonal anti-mouse AlexaFluor488-labeled IgG secondary antibody (5 μ g/mL, Abcam, Plc.) into each device, and then let this stand for 15 min. Finally, we washed out each device using PBS and followed that by fluorescence intensity observation under a fluorescence microscope (Olympus, Co., Ltd.). We found that ZnO nanowires could collect EVs efficiently while ZnO/Al₂O₃ core-shell nanowires could collect EVs only slightly; these findings led us to conclude that the nanowire surface charge was the dominant factor.

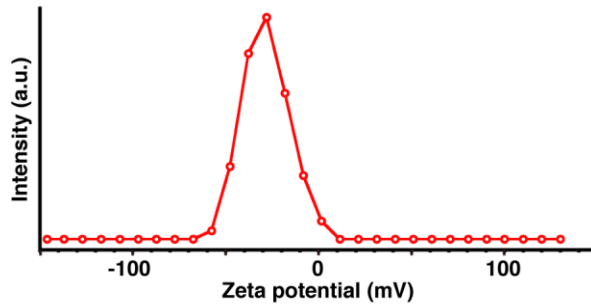


fig. S8. Zeta potential of EVs in urine. EV zeta potential was measured using a dynamic light scattering apparatus (Zetasizer Nano-ZS, Malvern Instruments, Ltd.). Mean zeta potential of EVs was -28.0 mV.

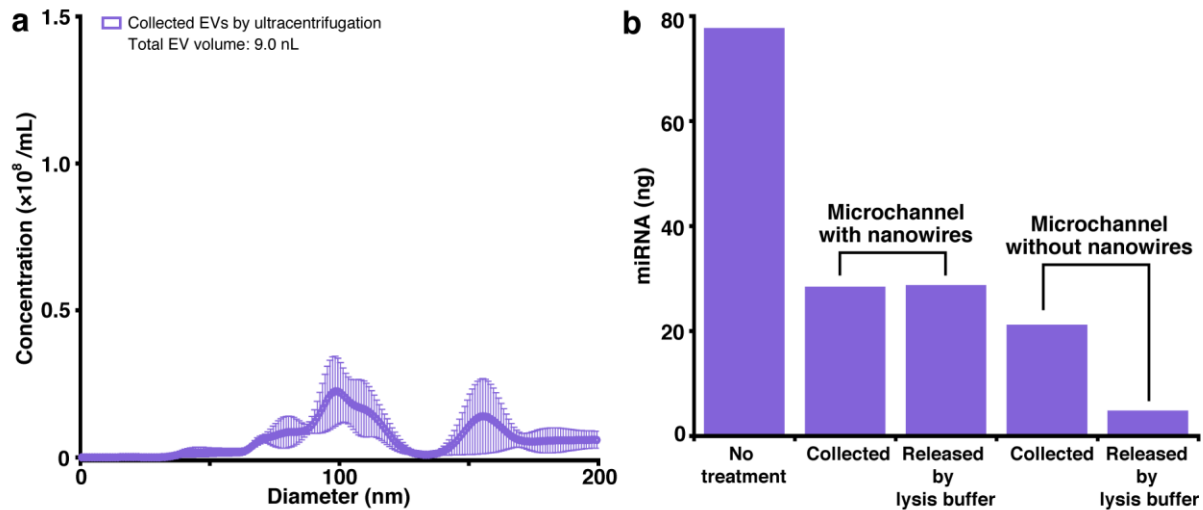


fig. S9. Size distribution of EVs collected by ultracentrifugation and EV-free miRNAs collected onto nanowires. (a) The concentration of collected EVs was $1.6 \times 10^9 \text{ mL}^{-1}$. Error bars show the standard deviation for a series of measurements ($N=3$). (b) Collected and released miRNAs quantities evaluated by the quantitative reverse transcription polymerase chain reaction (qRT-PCR). As EV-free miRNA, we used a 100-nM miRNA (sequence, uugcauagucacaaaagugauc). The designation “no treatment” represents the 100-nM miRNA quantity. Recovery rates of microchannels with and without nanowires were 100 and 23 %, respectively.

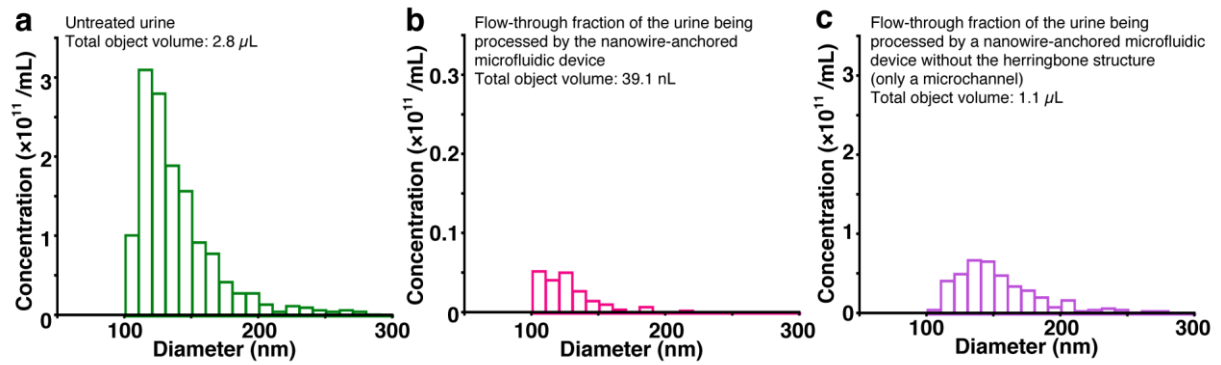


fig. S10. Size distribution of the urinary free-floating objects. The urinary free-floating object size distribution and concentration were measured using a nanoparticle detector (qNano, Meiwafofosis Co., Ltd.) with a 100 nm nanopore membrane (NP100, Meiwafofosis Co., Ltd.). **(a)** The urinary free-floating objects in the untreated urine; concentration was 1.4×10^{12} mL⁻¹. **(b)** The urinary free-floating objects in the flow-through fraction of the urine being processed by the nanowire-anchored microfluidic device; concentration was 2.4×10^{10} mL⁻¹ (capturing efficiency, 99%). **(c)** The urinary free-floating objects in the flow-through fraction of the urine being processed by a nanowire-anchored microfluidic device without the herringbone structure (only a microchannel); concentration was 4.3×10^{11} mL⁻¹ (capturing efficiency, 61%).

movie S1. EV collection followed by miRNA extraction in urine using the nanowire-anchored microfluidic device.

data S1. Logarithmic signal intensities in noncancer miRNAs with those in cancer miRNAs.